Cerebral Cortex, June 2016;26: 2715–2727

doi: 10.1093/cercor/bhv127
Advance Access Publication Date: 4 June 2015
Original Article

ORIGINAL ARTICLE

Differential Recruitment of Dentate Gyrus Interneuron Types by Commissural Versus Perforant Pathways

Tsan-Ting Hsu[1], Cheng-Ta Lee[1], Ming-Hong Tai[3], and Cheng-Chang Lien[1,2]

[1]Institute of Neuroscience, [2]Brain Research Center, National Yang-Ming University, Taipei, Taiwan, and [3]Institute of Biomedical Sciences, National Sun Yat-Sen University, Kaohsiung, Taiwan

Address correspondence to Ming-Hong Tai, Institute of Biomedical Sciences, National Sun Yat-Sen University, 70, Lienhai Road, Kaohsiung 804, Taiwan. Email: minghongtai@gmail.com; Cheng-Chang Lien, Institute of Neuroscience, National Yang-Ming University, 155, Section 2, Li-Nong Street, Taipei 112, Taiwan. Email: cclien@ym.edu.tw

Tsan-Ting Hsu and Cheng-Ta Lee contributed equally to this work.

Abstract

Gamma-aminobutyric acidergic (GABAergic) interneurons (INs) in the dentate gyrus (DG) provide inhibitory control to granule cell (GC) activity and thus gate incoming signals to the hippocampus. However, how various IN subtypes inhibit GCs in response to different excitatory input pathways remains mostly unknown. By using electrophysiology and optogenetics, we investigated neurotransmission of the hilar commissural pathway (COM) and the medial perforant path (MPP) to the DG in acutely prepared mouse slices. We found that the short-term dynamics of excitatory COM–GC and MPP–GC synapses was similar, but that the dynamics of COM- and MPP-mediated inhibition measured in GCs was remarkably different, during theta-frequency stimulation. This resulted in the increased inhibition–excitation (I/E) ratios in single GCs for COM stimulation, but decreased I/E ratios for MPP stimulation. Further analysis of pathway-specific responses in identified INs revealed that basket cell-like INs, total molecular layer- and molecular layer-like cells, received greater excitation and were more reliably recruited by the COM than by the MPP inputs. In contrast, hilar perforant path-associated and hilar commissural–associational pathway-related-like cells were minimally activated by both inputs. These results demonstrate that distinct IN subtypes are preferentially recruited by different inputs to the DG, and reveal their relative contributions in COM-mediated feedforward inhibition.

Key words: GABA, granule cell, inhibition, mossy cell, optogenetics

Introduction

The dentate gyrus (DG) serves as a primary gate, filtering and processing sensory inputs entering the hippocampus (Amaral et al. 2007; Treves et al. 2008). Its principal neurons, granule cells (GCs), have low intrinsic excitability and fire sparsely both in vivo and ex vivo (Alme et al. 2010; Pernía-Andrade and Jonas 2014). Their sparse firing serves as a protective shield, protecting hippocampal circuits against runaway excitation (Behr et al. 1998; Coulter and Carlson 2007). Most importantly, it enables the transformation of massive overlapping cortical information into the discrete representations that are required for rapid pattern separation (Leutgeb et al. 2007). In addition to low intrinsic excitability (Schmidt-Hieber et al. 2007; Krueppel et al. 2011; Chiang et al. 2012), inhibitory circuit mechanisms also have been shown to contribute to the sparse activation of GCs. For instance, the excitatory input from the medial entorhinal cortex (MEC), called the medial perforant path (MPP), is known to recruit fast-spiking basket cells (BCs), thereby providing feedforward inhibition onto GCs (Ewell and Jones 2010; Dieni et al. 2013; Liu et al. 2014).

However, several important outstanding questions remain unanswered with respect to the circuit-driven inhibition. First, there are multiple classes of interneurons (INs) in the DG (Han et al. 1993; Freund and Buzsáki 1996; Mott et al. 1997; Hosp et al. 2014; Liu et al. 2014); apart from fast-spiking BCs, do other IN subtypes contribute to GC input–output transformations? Second, whether there are long-range excitatory afferents from other brain regions (Soriano and Frotscher 1994; Boulland et al.

2009; Vivar et al. 2012) and what their cellular targets are, if so. One notable long-range excitatory afferent projecting to the DG is the commissural pathway (COM), which originates from mossy cells (MCs) in the contralateral hilus, and innervates the proximal dendrites of GCs within the inner one-third molecular layer (IML; West et al. 1979; Soriano and Frotscher 1994; Buckmaster et al. 1996; Scharfman and Myers 2013). Previous in vivo studies showed that COM activation exerts a suppressive effect on concurrent perforant path (PP)-evoked population spikes in the DG through feedforward inhibition (Buzsáki and Czéh 1981; Buzsáki and Eidelberg 1981; Bilkey and Goddard 1987). The COM–PP inputs thus compose a control circuit to regulate patterns of information flow. However, a direct connection of COM afferents to specific inhibitory IN types remains poorly understood.

The COM axonal projections substantially overlap with those from the supramammillary nucleus (SuM) in the IML (Boulland et al. 2009; Soussi et al. 2010; Kohara et al. 2014). In addition, hilar MCs also form ipsilateral projections (i.e., the associational pathway) to innervate the proximal dendrites of GCs within the IML. Therefore, it is not possible to differentially activate these excitatory pathways with conventional electrical stimulation. Accordingly, here we used cell type-specific optogenetic tools to selectively activate the MPP and COM (Yizhar et al. 2011; Chancey et al. 2014). We found that photostimulation of each of these 2 inputs resulted in distinct inhibition patterns in GCs. Further analysis of pathway-specific responses revealed that BC-like cells were reliably activated by both inputs. However, 2 dendrite-targeting IN subtypes, the total molecular layer (TML)- and molecular layer (ML)-like cells, received greater excitation from the COM and were more reliably recruited by the COM than by the MPP inputs. Taken together, our results indicate that in addition to BC-like cells, TML- and ML-like cells substantially contribute to COM-mediated inhibition.

Materials and Methods

Animals

All animals were handled in accordance with the national and institutional guidelines, and protocols were approved by the Animal Care and Use Committee of the National Yang-Ming University. All *Grik4-cre* animals used for electrophysiology were adult (2–5 months old) transgenic hemizygote mice (stock #006474; Jackson Laboratory, Bar Harbor, ME, USA). To target excitatory neurons, we used wild-type mice with a C57BL/6 genetic background. Mice of both sexes of the above strains were included in these studies.

Virus

We generated an adeno-associated virus serotype 5 (AAV5) carrying Cre-inducible channelrhodopsin-2 (ChR2)-enhanced yellow fluorescent protein (eYFP) transgene AAV5-EF1α-DIO-hChR2 (H134R)-eYFP-WPRE-pA provided by Dr Karl Deisseroth (Stanford University, Stanford, CA, USA) to target expression of hilar MCs. The AAV5 packaging (pLT-RC03) and adenovirus helper (pHGTI-Adeno1) constructs were gifts from Dr Jeng-Shin Lee (Harvard Gene Therapy Initiative, Harvard Medical School, Boston, MA, USA). To target the excitatory neurons in the MEC, we used the AAV5 carrying CaMKIIα promoter-driven ChR2 tagged with mCherry [AAV5-CaMKIIα-hChR2(H134R)-mCherry-WPRE-pA], which was produced by the University of North Carolina Vector Core Facilities, Chapel Hill, NC, USA.

Stereotaxic Injection

Mice (postnatal day >30) were anesthetized with 4% isoflurane (vol/vol; Halocarbon Laboratories, North Augusta, SC, USA) in 100% oxygen in an induction chamber (air flow rate: 4 mL/min), and their heads were shaved for further operation. Mice were placed onto the stereotaxic frame (Stoelting Co., Wood Dale, IL, USA). The mouths and noses of the mice were covered by an anesthetizing mask, supplied with approximately 1.5% isoflurane air flow (4 mL/min). A homeothermic blanket (Panlab Harvard Apparatus, Barcelona, Spain) was placed below the mice to keep the body temperature constant (34 °C). After securing the head with 2 ear bars, 75% ethanol was used to sterilize the surgical area and the eyes were protected by ophthalmic gel. To target hilar MCs of the dorsal hippocampus, a midline scalp incision (~1 cm) was made with scissors and the skin pulled aside to expose the skull. A small craniotomy (coordinates from Bregma: anteroposterior (AP): −2 mm; mediolateral (ML): ±1.3 mm) was made directly over the dorsal hippocampus. The viral vector was delivered through the craniotomy to the 2 locations within the dorsal hippocampus (dorsoventral (DV): −2 and −1.8 mm), using a 10-μL NanoFil syringe (World Precision Instruments, Sarasota, FL, USA) and a 35-gauge beveled metal needle. Injection volume (0.5 μL at each location) and flow rate (0.1 μL/min) were controlled with a nanopump Controller (KD Scientific, Holliston, MA, USA). After viral injection, the needle was left in place 0.2 mm above the injection sites for 10 min before it was withdrawn slowly. Similar procedures were made for targeting excitatory neurons in the MEC except that the craniotomy and subsequent viral injection were delivered to the 2 locations within the MEC (coordinates from Bregma: AP: −4.7 mm; ML: ±3.3 mm; DV: −3.5 and −3.3 mm). After viral injection, the incision was closed by suturing and mice were placed back to the home cage for recovery. All animals were allowed at least 3 weeks of rest before the next experimental stage was commenced, ensuring complete recovery and sufficient gene expression.

Preparation of Brain Slices

After at least 3 weeks of recovery, virus-injected mice (postnatal day >51) were anesthetized with isoflurane and transcardially perfused with cold carbogenated (95% O_2 and 5% CO_2) sucrose solution (~30 mL) containing (in mM): 87 NaCl, 25 $NaHCO_3$, 1.25 NaH_2PO_4, 2.5 KCl, 10 glucose, 75 sucrose, 0.5 $CaCl_2$, and 7 $MgCl_2$. The brain was dissected out and coronal slices (300 μm) were prepared in the same carbogenated sucrose solution using a vibrating tissue slicer (DTK-1000; Dosaka, Kyoto, Japan) under a dim red light. Following sectioning, slices were incubated in a holding chamber filled with the carbogenated sucrose solution at 34°C for about 25 min, then shifted to room temperature for further experiments.

Electrophysiology and Optical Stimulation

For experiments, individual slices were transferred to a submerged chamber and were continuously perfused with carbogenated artificial cerebrospinal fluid (ACSF) containing the following (in mM): 125 NaCl, 25 $NaHCO_3$, 1.25 NaH_2PO_4, 2.5 KCl, 25 glucose, 2 $CaCl_2$, and 1 $MgCl_2$. The ChR2-eYFP or ChR2-mCherry expression pattern was confirmed by epifluorescence and neurons were visually selected for recordings under infrared Dodt gradient contrast optics (Leica DM6000 CFS, Leica Microsystems, Wetzlar, Germany). Axonal fibers expressing ChR2 were stimulated with 473-nm light, which was delivered from a 200-μm multimode optical fiber (0.39 numerical aperture, Thorlabs,

Newton, NJ, USA) coupled with a 473-nm, diode-pumped, solid-state laser (OEM Laser Systems, Midvale, UT, USA). The distance between the tip of optic fiber and the recorded single cell/pair was approximately 100–300 μm, and the distance between the recorded pair was smaller than the tip diameter (200 μm). The area of photostimulation was large enough to cover the entire DG under this condition. Near-maximum light intensity was also used to avoid the possible difference of light intensity due to displacement of fiber between recorded pair. The onset and duration of light pulses were detected by a GaP Photodiode (wavelength range: 150–550 nm, 1 ns rise time, Thorlabs) placed near the submerged chamber. For cell-attached and whole-cell patch-clamp recordings, pipettes (4–8 MΩ) pulled from borosilicate glass tubing (outer diameter, 1.5 mm; inner diameter, 0.86 mm; Harvard Apparatus, Holliston, MA, USA) were filled with low Cl^- internal solution, containing the following (in mM): 136.8 K-gluconate, 7.2 KCl, 0.2 EGTA, 4 MgATP, 10 HEPES, 7 Na_2-phosphocreatine, 0.5 Na_3GTP (pH 7.3 with KOH), and 0.5% biocytin (wt/vol; Life Technologies, Grand Island, NY, USA). To measure the inhibitory (I)–excitatory (E) conductance ratio, Cs-based intracellular solution was used, containing (in mM): 121.5 $CsMeSO_3$, 0.1 EGTA, 4 $MgCl_2$, 13.5 $CsCl_2$, 10 HEPES, 5 QX-314 bromide, 2 Na_2ATP, 10 Na_2-phosphoreatine, 0.3 Na_3GTP, and 0.2% biocytin (wt/vol). Excitatory and inhibitory synaptic responses were evoked by 10 Hz train photostimulation (light pulse duration, 5 ms; intertrain interval, 15 s). Pipette capacitance and series resistance were compensated (100% in current clamp and 70% in voltage clamp). For interactions of COM and PP experiments, transverse slices containing the ventral DG were selected because the PP projection from the EC can be largely preserved in the subiculum in this preparation. The PP fibers were stimulated for 0.1 ms with constant current (range of 10–1000 μA) using a monopolar electrode placed in the subiculum to avoid the direct activation of DG IN axons. Field recordings were performed with ACSF-filled patch pipettes (with a resistance of <1 MΩ). Data were recorded with Multiclamp 700B amplifiers (Molecular Devices, Sunnyvale, CA, USA), filtered at 4 kHz, and sampled at 10 kHz with a Digidata 1440 interface (Molecular Devices) controlled by pClamp 10.2 software (Molecular Devices). All recordings were conducted in dim light conditions. The recording temperature was 23 ± 2 °C in the majority of experiments and 34 ± 2 °C in subsets (Fig. 6 and see Supplementary Fig. 5).

Immunohistochemistry

To identify the recorded neurons (filled with 0.2 or 0.5% biocytin), brain slices were fixed overnight with 4% paraformaldehyde (wt/vol) in phosphate-buffered saline (PBS). After washing with PBS 3 times, slices were incubated with streptavidin-conjugated Alexa Fluor 594 or 488 (1 : 400; Life Technologies) in PBS and 0.3% Triton X-100 (vol/vol; USB Co., Cleveland, OH, USA) overnight at 4 °C. After washing 6 times with PBS, slices were mounted onto slides with mounting medium Vectashield (Vector Laboratories, Burlingame, CA, USA). For nuclear staining, slices were incubated with 4′,6-diamidino-2-phenylindole (DAPI; 1 : 5000; Life Technologies) for 15 min before finally washing with PBS 6 times. Labeled cells were imaged using a confocal/two-photon laser excitation microscope (Leica SP5 module, Leica Microsystems). Confocal image stacks were reconstructed with Neuromantic 1.6.5 software (developed by Darren Myatt, University of Reading, Reading, Berkshire, UK). To characterize Cre recombinase expression in the *Grik4-cre* mouse line, the ROSA26-*LacZ* reporter mouse line was crossed with the *Grik4-cre* mouse. The offspring, which contained both *cre* and *lacZ* genes, were used for X-gal staining. In brief, mice were anesthetized with pentobarbital (50 μg/mL) and transcardially perfused with PBS, followed by 4% paraformaldehyde in PBS. The fixed brain was removed and post-fixed in 4% paraformaldehyde for an additional 6 h. After dehydrating with 30% sucrose in PBS, the fixed brain was embedded in optimal cutting temperature compound (Sakura Finetek Japan Co., Tokyo, Japan) for cryosectioning into 30 μm coronal slices. The slices were incubated with X-gal working solution containing (in mM): 10 phosphate buffer, 150 NaCl, 3.5 $K_3Fe(CN)_6$, 3.5 $K_4Fe(CN)_6$, 1 $MgCl_2$, 0.3 chloroquine, 0.01% Na-deoxycholate (wt/vol), 0.2% octyl-1-phenoxypolyethoxyethanol (NP-40, vol/vol), and 0.1% X-gal (wt/vol) at 30 °C for 16 h, followed by intensifying solution (0.3 mM chloroquine in PBS) for an additional 8 h. After washing the slices with PBS 3 times, slices were mounted onto slides with the mounting medium Entellan® new (Merck, Darmstadt, Germany). X-gal signals were visualized and photographed using a stereoscopic microscope (Leica EZ4D, Leica Microsystems).

Chemicals and Drugs

The *N*-methyl-D-aspartate receptor (NMDAR) antagonist D-2-amino-5-phosphonopentanoate (D-AP5), α-amino-3-hydroxy-5-methyl-4-isoxazolepropionic acid (AMPA)/kainate receptor-specific antagonist 6-cyano-7-nitroquinoxaline-2,3-dione (CNQX), and the sodium channel antagonists tetradotoxin citrate (TTX) and QX-314 bromide were purchased from Ascent Scientific, Avonmouth, UK. X-gal was purchased from GMbiolab Co., Taichung, Taiwan. NP-40 used in X-gal staining was purchased from BioShop Canada, Inc., Burlington, ON, Canada. All other reagents were purchased from Sigma-Aldrich Co., Saint Louis, MO, USA.

Data Analysis and Statistics

Data were analyzed using Clampfit 10.2 (Molecular Devices) and Prism 5.0 (GraphPad). The onset of the synaptic response was determined by the intersection of a line through the 20% and 80% points of the rising phase of the excitatory postsynaptic current (EPSC) and the baseline. To calibrate evoked inhibitory postsynaptic currents (IPSCs) during successive 10 Hz photostimulations, a single exponential fit of the decay of the preceding IPSC was subtracted from the subsequent IPSC. The IPSC amplitude after subtraction was used for the conductance calculation. To calculate the conductance, the EPSC and the IPSC were divided by their driving forces, respectively. The input resistance (R_{in}) was measured as the ratio of the steady-state (last 100 ms of the 1-s pulse; average of 1–4 traces) voltage response and the 1-s hyperpolarizing current pulse amplitude (100 pA). Spike delay was calculated as the time elapsed from the onset of photostimulation to the peak of action current in cell-attached recordings. Data are presented as mean ± standard error of mean (SEM). Error bars in figures also show SEMs. Statistical significance was tested using the Mann–Whitney rank-sum test or two-way repeated-measures ANOVA using GraphPad Prism 5.0. Significance levels were set at $P < 0.05$ (*), $P < 0.01$ (**), and $P < 0.001$ (***) for the entire family of comparisons.

Results

Selective ChR2 Expression in the COM or MPP

To selectively investigate neurotransmission of the COM and the MPP to the DG, we applied optogenetic control strategies. To target the COM, we unilaterally injected a Cre-inducible AAV expression vector serotype 5 [AAV5-EF1α-DIO-hChR2(H134R)-eYFP-WPRE-pA] into the hilar region of the dorsal hippocampus of *Grik4-cre* hemizygous mice (Fig. 1A). We first assessed the

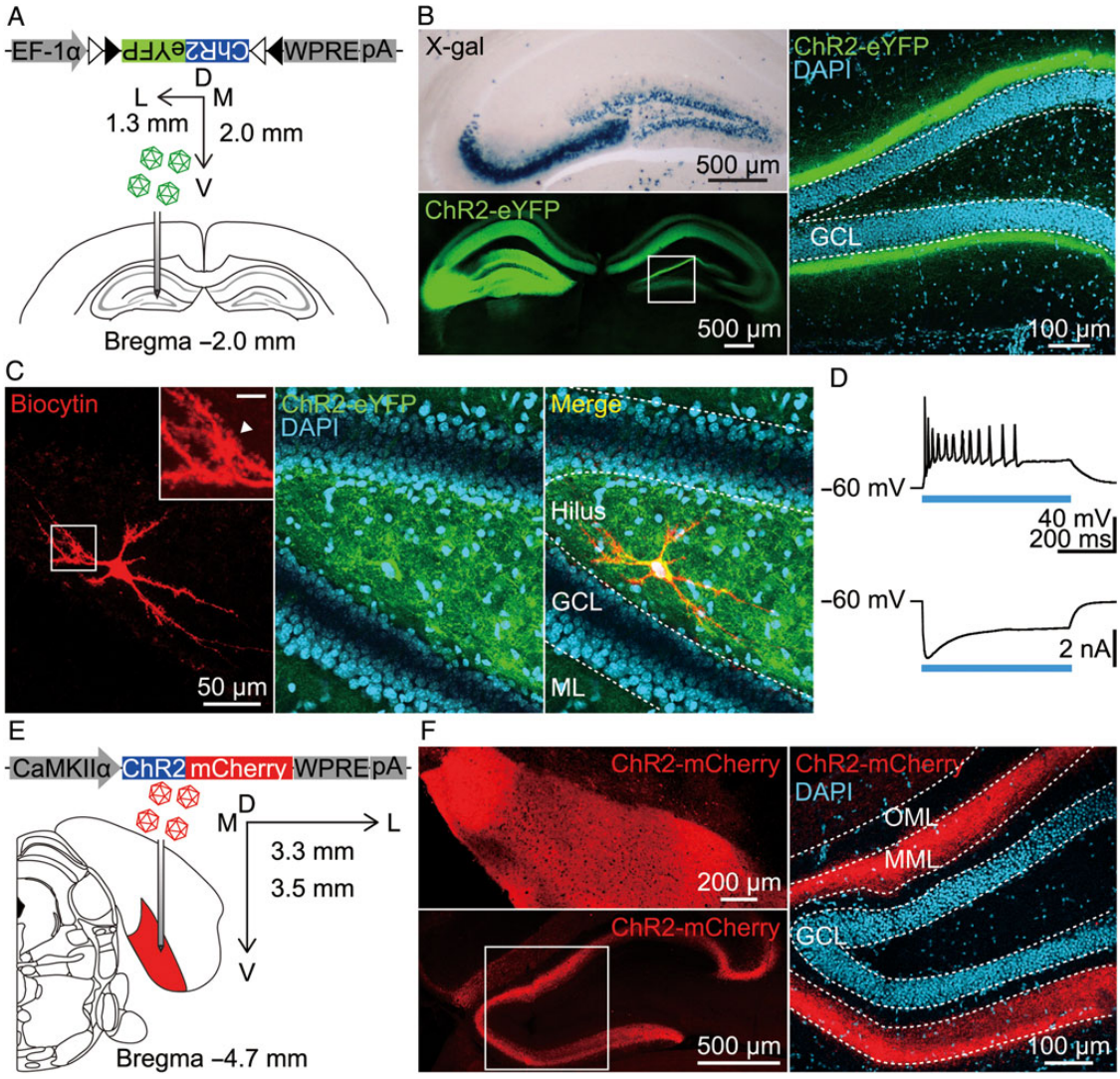

Figure 1. ChR2 expression in the COM and the MPP to the DG. (*A*) Schematic diagram illustrates a coronal section from a *Grik4-cre* mouse injected unilaterally with a viral vector AAV5-EF1α-DIO-ChR2-eYFP into the hilar region of the dorsal hippocampus. Axis: L, lateral; V, ventral; M, medial; D, dorsal. (*B*) Left upper, coronal section stained with X-gal from the dorsal hippocampus of *Grik4-cre* mice crossed with the *loxP*-flanked *Rosa26LacZ* reporter line. Left lower, fluorescence image of ChR2-eYFP expression in the dorsal hippocampus; the boxed area is shown at a higher magnification on the right. The borders of the GCL are outlined. Note the laminated ChR2-eYFP expression in the IML of the contralateral DG. (*C*) Left, the morphology of a biocytin-filled MC. The boxed area is shown at a higher magnification in the inset; arrowhead indicates the thorny excrescences; scale bar in the inset: 10 μm. Middle, fluorescence image of ChR2-eYFP expression in the hilar region. Right, the merged image. (*D*) Top, photostimulation (0.8 mW) evoked spikes in an MC (shown in *C*) in current clamp. Membrane voltage is indicated. Bottom, ChR2-mediated photocurrent was recorded in voltage clamp (held at –60 mV) upon photostimulation (1.1 mW). The blue bar indicates the light pulse. (*E*) Schematic diagram illustrates a coronal section from a wild-type mouse injected with a viral vector AAV5-CaMKIIα-ChR2-mCherry into the MEC. (*F*) Left upper, ChR2-mCherry expression at the injection site MEC. Left lower, ChR2-mCherry expression in the hippocampus; the boxed area is shown at a higher magnification on the right. Right, fluorescent image reveals the laminated ChR2-mCherry expression in the MML of the DG. DAPI staining (*B*,*C*,*F*) defines the area of the GCL.

distribution and efficiency of Cre/loxP recombination in this transgenic line by crossing it with the ROSA26-*LacZ* reporter mouse and analyzing X-gal-stained brain sections from *cre/lacZ* double-transgenic mice (see Materials and Methods). As reported earlier (Nakazawa et al. 2002), Cre recombinase activities were detected in CA3 pyramidal neurons, GCs, and neurons in the hilar region (Fig. 1*B*, left upper). Three weeks after injection, the ChR2-eYFP fusion protein was expressed in CA3 pyramidal neurons, GCs, putative MCs, and their axonal projections on the ipsilateral side as well as the COM axonal projections across the hippocampal commissure (Fig. 1*B*, left lower). Notably, ChR2-eYFP was densely expressed along the IML of the contralateral side of the dorsal DG (Fig. 1*B*, right and see Supplementary Fig. 1), consistent with previous reports that MC axonal bundles primarily target the proximal dendrites of contralateral GCs (West et al. 1979; Buckmaster et al. 1996; Scharfman and Myers 2013). Also, it is worth noting that we did not observe ChR2-eYFP expression in the IML of the contralateral DG when the viral transduction was mainly restricted in the CA3 area of the injection site (see Supplementary Fig. 2). To characterize the putative ChR2-eYFP-labeled MCs in the hilus, we filled them with biocytin during whole-cell recordings and correlated their morphologies with their intrinsic properties. In the injection site, the biocytin-filled cells that expressed ChR2-eYFP had characteristic MC morphology including thorny excrescences on proximal dendrites (Fig. 1*C*, arrowhead). When the ChR2-eYFP-labeled MC was illuminated with a blue light pulse in the presence of the AMPA receptor-specific antagonist CNQX (10 μM), it

depolarized and generated spikes in current clamp (Fig. 1*D*, upper). Similarly, an inward ChR2-mediated photocurrent (peak amplitude, 1391 ± 714 pA, $n = 4$) was detected in voltage clamp (Fig. 1*D*, lower). To target the MPP, we injected an AAV5 encoding ChR2-mCherry under the control of the CaMKIIα promoter [AAV5-CaMKIIα-hChR2(H134R)-mCherry] into the MEC of wild-type mice (Fig. 1*E*). Three weeks after injection, ChR2-mCherry-expressing neurons and their axonal projections were observed around the MEC injection site (Fig. 1*F*, left upper) and the dorsal hippocampus (Fig. 1*F*, left lower). Notably, ChR2-mCherry-labeled fibers were clearly demarcated in part of the IML and the medial one-third molecular layer (MML), indicating selective ChR2 expression in the MPP (Fig. 1*F*, right; also see Supplementary Fig. 1).

GCs Receive More Inhibition Than Excitation From the COM

To determine the proper intensity for photostimulation, we varied the light intensities (duration 5 ms) and recorded the optically evoked inward EPSCs in GCs ($V_{hold} = -75$ mV, near the IPSC reversal potential; $[Cl^-]_i = 7.2$ mM). The GCs were filled with biocytin during recordings and were identified post hoc (Fig. 2*A*). Analysis of the input–output relationship showed that the EPSC amplitude was saturated at high light intensities (Fig. 2*B*). The near-maximal light intensity (blue area in Fig. 2*B*; 30–60 mW for COM–GC and 53–60 mW for MPP–GC) was chosen for subsequent experiments to ensure maximum recruitment of INs during light stimulation. In a subset of experiments, we chose 2 intermediate

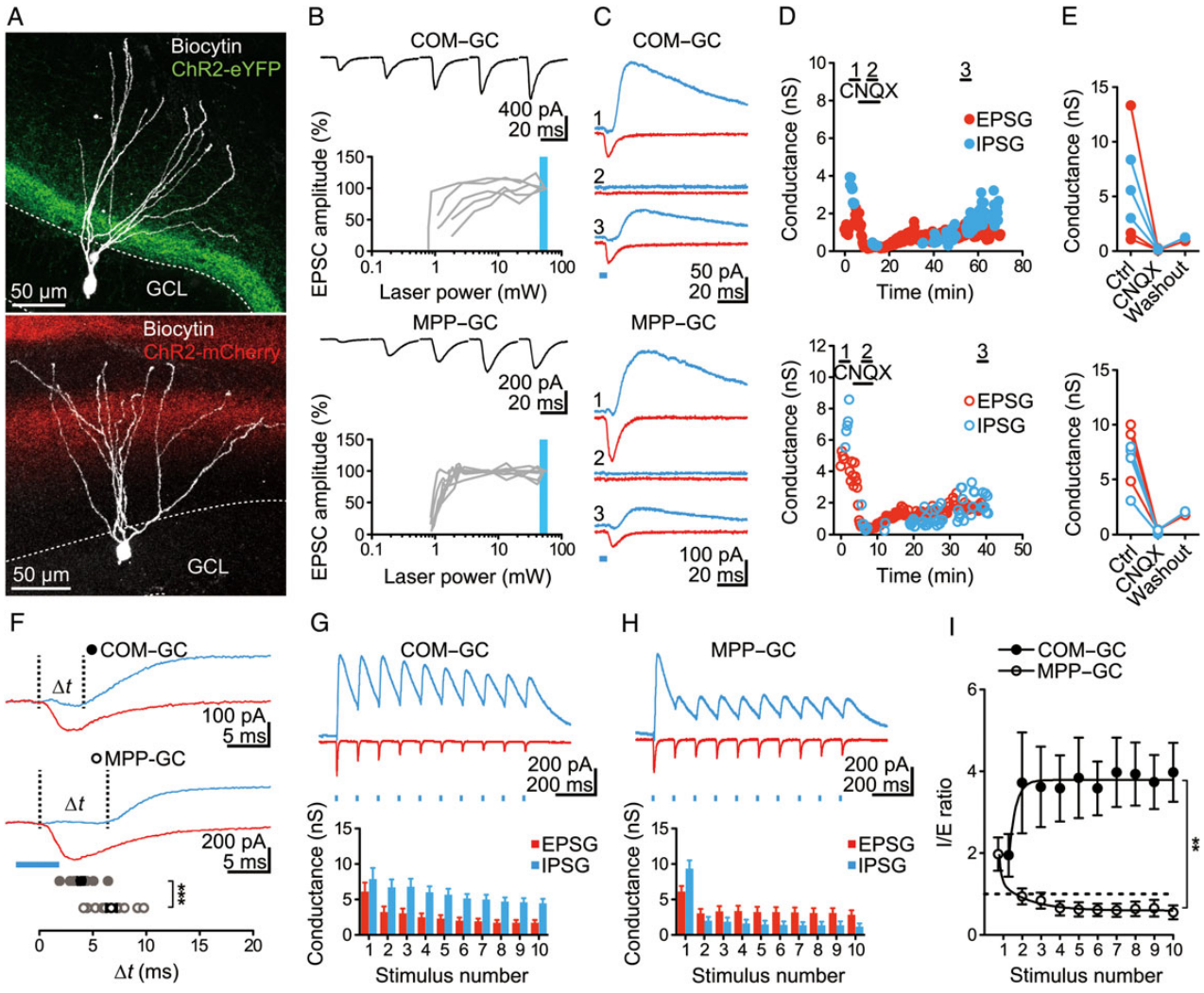

Figure 2. Distinct I/E ratios at COM–GC and MPP–GC synapses during repetitive stimulation. (*A*) Confocal image stacks show selective ChR2-eYFP (upper, green) and ChR2-mCherry (lower, red) expression in the COM and MPP, respectively. Images were superimposed with biocytin-labeled GCs (white). (*B*) Photostimulation of COM (upper) or MPP (lower) with increasing light intensities corresponding to the increments of EPSCs ($V_{hold} = -75$ mV) in GCs. Photostimulation was applied every 15 s. The maximal light intensity in the blue area was used for subsequent experiments. Representative traces of averaged EPSCs evoked by blue light at 5 levels of laser intensity were shown above the input–output curves. (*C*) Example traces of light-evoked EPSC (red, $V_{hold} = -25$ mV) and IPSC (blue, $V_{hold} = 10$ mV) recorded in a GC in the continuous presence of the NMDAR blocker D-AP5 (50 μM). Photostimulation was applied every 15 s. (1) ACSF; (2) application of the AMPA receptor blocker CNQX (10 μM); and (3) washout. Upper: COM–GC synapse. Lower: MPP–GC synapse. (*D*) Plots of experiments shown in (*C*). Application of CNQX and the sample traces shown in (*C*) are indicated by bars. Upper, COM–GC EPSG: red-filled circles; COM–GC IPSG: blue-filled circles. Lower, MPP–GC EPSG: red open circles; MPP–GC IPSG: blue open circles. (*E*) Summary plots of CNQX effect on light-evoked EPSG and IPSG at the COM (upper) or MPP (lower). Symbols are the same as in (*D*). (*F*) Synaptic delay (Δt) between the light-evoked IPSC and EPSC at the COM (upper) or MPP (lower). The vertical dashed lines mark the onset of EPSC and IPSC. ***$P < 0.001$. (*G*,*H*) Top traces: EPSCs (red, $V_{hold} = -25$ mV) and IPSCs (blue, $V_{hold} = 10$ mV) evoked by 10 Hz photostimulation of COM (*G*) or MPP (*H*). Bottom, summary of EPSGs and IPSGs during theta-frequency photostimulation of COM (*G*, $n = 12$) or MPP (*H*, $n = 11$). Photostimulation train was applied every 15 s. (*I*) Summary of the I/E ratio versus the stimulus number during 10 Hz photostimulation of COM or MPP. Dashed lines, I/E ratio = 1; $n = 12$ for COM–GC; $n = 11$ for MPP–GC. **$P < 0.01$. Data are expressed as mean ± SEM.

Table 1 Properties of EPSC and IPSC in GCs

Input	Synaptic delay[a] (ms)	20–80% Rise time (ms)	Decay time constant (ms)
EPSC			
COM (13)	2.9 ± 0.1	1.0 ± 0.1	4.6 ± 0.1
MPP (12)	3.9 ± 0.2	1.8 ± 0.1	5.9 ± 0.4
IPSC			
COM (13)	6.8 ± 0.3	5.3 ± 0.2	96.7 ± 5.9
MPP (12)	10.6 ± 0.5	5.7 ± 0.5	92.8 ± 7.3

Note: Numbers of cells are given in parentheses.
[a]Synaptic delay was calculated as the time elapsed from the onset of photostimulation to the onset of first EPSC or IPSC.

holding potentials (V_{hold} = −25 mV, near the experimentally determined IPSC reversal potential and V_{hold} = 10 mV, near the experimentally EPSC reversal potential; see Supplementary Fig. 3) with Cs-based internal solution ($[Cl^-]_i$ = 35 mM; see Materials and Methods) to measure EPSCs and IPSCs, respectively. To avoid contamination of NMDAR-mediated currents, we measured IPSCs and I/E ratios in the presence of the NMDAR blocker D-AP5 (50 μM; Fig. 2*C*). Because the same driving forces (35 mV) were used for excitation and inhibition, we can thus directly compare excitatory and inhibitory conductances. We recorded optically evoked EPSCs (215 ± 43 pA; n = 13 in the COM group; 215 ± 28 pA; n = 12 in the MPP group; V_{hold} = −25 mV) and IPSCs (277 ± 55 pA; n = 13 in the COM group; 327 ± 41 pA; n = 12 in the MPP group; V_{hold} = 10 mV). We know that the kinetic properties of EPSCs are related to the electrotonic distance of the synapses, which is dependent on the laminar organization of the inputs. Consistent with this notion, the 20–80% rise time and decay time constant of evoked EPSCs at the COM were significantly shorter than those at the MPP (20–80% rise time, COM, 1.0 ± 0.1 ms, n = 13 vs. MPP, 1.8 ± 0.1 ms, n = 12; P < 0.0001; decay time constant, COM, 4.6 ± 0.1 ms, n = 13 vs. MPP, 5.9 ± 0.4 ms, n = 12; P = 0.006; Table 1). In a subset of experiments (Fig. 2*C*–*E*), bath application of CNQX (10 μM) abolished light-evoked EPSCs and IPSCs at both synapses, confirming that the EPSCs are indeed glutamatergic, AMPA/kainate receptor-mediated and that the IPSCs are disynaptic.

We next examined the synaptic delay of the EPSC following photostimulation. Synaptic delay was calculated from the time of the onset of photostimulation to the onset of the EPSC. The average delay of the EPSC at the COM–GC and MPP–GC synapses was 2.9 ± 0.1 ms (n = 13) and 3.9 ± 0.2 ms (n = 12), respectively (Table 1). Because EPSCs significantly preceded IPSCs, we thus measured the delay (Δt) of the IPSC relative to the EPSC following photostimulation (Fig. 2*F*). The average Δt of the IPSC at the COM–GC and MPP–GC synapses was 3.9 ± 0.3 ms (n = 13) and 6.7 ± 0.5 ms (n = 12), respectively. A significantly longer Δt at the MPP–GC synapse (MPP vs. COM; P = 0.0003, Mann–Whitney rank-sum test; Fig. 2*F*) suggests that INs were activated with longer excitatory postsynaptic potential (EPSP)-spike latencies (Maccaferri and Dingledine 2002) or recruited through recurrent excitatory inputs (Bartos et al. 2011).

Dentate GCs have been shown to receive coherent theta (4–10 Hz)-band EPSCs in vivo (Pernía-Andrade and Jonas 2014). We finally investigated the synaptic excitation and inhibition during successive inputs coming from either the COM or the MPP. To compare synaptic inhibitory drive across different levels of excitatory drive, we derived their corresponding peak excitatory and inhibitory postsynaptic conductances (i.e., IPSG vs. EPSG) and expressed inhibition relative to excitation [IPSG/EPSG (I/E) ratio]. When 10 brief (5 ms) light pulses at 10 Hz were delivered to the COM, the EPSCs depressed much more than the IPSCs (Fig. 2*G*), yielding higher I/E ratios in GCs (see Supplementary Fig. 4 for IPSC calibration). In contrast, the IPSCs significantly depressed, whereas the EPSCs remained relatively constant, during 10 Hz photostimulation of MPP (Fig. 2*H*). This results in striking facilitation in the I/E ratio at the COM–GC synapse, but depression at the MPP–GC synapse during repetitive stimulation (Fig. 2*I*, n = 12 for COM–GC and n = 11 for MPP–GC; P = 0.0027, two-way repeated-measures ANOVA). When comparing the I/E ratio at the 10th light pulse, the mean I/E ratio at the COM (4.2 ± 0.7, n = 12) is about 7-fold greater than that at the MPP (0.6 ± 0.2, n = 11). Note that the higher I/E ratios at the COM when compared with the MPP are also observed when recordings are made at physiological temperature (see Supplementary Fig. 5). Collectively, synaptic dynamics of IPSCs at the COM distinct from that at the MPP suggests that activation of COM and MPP pathways may differentially recruit different IN populations.

Comparison of COM- and MPP-mediated EPSCs Across Various IN Types

To dissect afferent-driven γ-aminobutyric acidergic (GABAergic) transmission onto GCs, we directly investigated the excitatory input to different types of INs. Patch-clamp whole-cell recordings were obtained from INs located near the border between the granule cell layer (GCL) and hilus or in the ML. To normalize ChR2 expression levels between slices, we simultaneously recorded pairs of a local IN and an adjacent GC in the DG in brain slices (Fig. 3*A*,*B*). The critical advantage of this simultaneous paired-recording technique is that it enables the direct comparison of synaptic input strength to 2 cells, while stimulating an identical group of axons (Lee et al. 2013). We measured the amplitude of the light-evoked EPSC in both cells (V_{hold} = −75 mV near the IPSC reversal potential; $[Cl^-]_i$ = 7.2 mM) and computed its normalized values. To minimize in-group heterogeneity due to differing maturation stages among GCs, only GCs with an R_{in} lower than 600 MΩ (corresponding to mature GCs, Schmidt-Hieber et al. 2004; Vivar et al. 2012; Dieni et al. 2013) were included for analysis (Fig. 3*C*). Overall, the R_{in} of GCs showed no difference between COM and MPP photostimulation groups (Fig. 3*C*; 279 ± 14 MΩ; n = 35 in the COM group vs. 308 ± 17 MΩ; n = 29 in the MPP group, P = 0.1379, Mann–Whitney rank-sum test).

On the basis of target selectivity of the axon, somatic locations, and physiological properties, 5 different IN subtypes have been distinguished in the DG, including BC-, hilar commissural–associational pathway-related (HICAP)-, hilar PP-associated (HIPP)-, TML-, and ML-like cells (Han et al. 1993; Freund and Buzsáki 1996; Mott et al. 1997; Hosp et al. 2014; Liu et al. 2014). A detailed characterization of the synaptic responses in all INs revealed single or multiple EPSC events following each light pulse (see Supplementary Fig. 6). To investigate monosynaptic connections, we selectively analyzed the first EPSCs for all experiments. The synaptic delays of COM- and MPP-mediated EPSCs in all IN subtypes were similar to those in GCs, which were known to receive monosynaptic transmission from the COM and MPP (Table 2). Note that these synaptic delays were shorter than those measured in the presence of TTX (1 μM) and 4-aminopyridine (4-AP, 1 mM; COM, 3.1 ± 0.3 ms and MPP, 4.9 ± 0.2 ms in control vs. COM, 6.1 ± 0.7 ms and MPP, 9.5 ± 1.0 ms in the TTX and 4-AP; see Supplementary Fig. 7), confirming monosynaptic transmission between COM and INs and between MPP and INs.

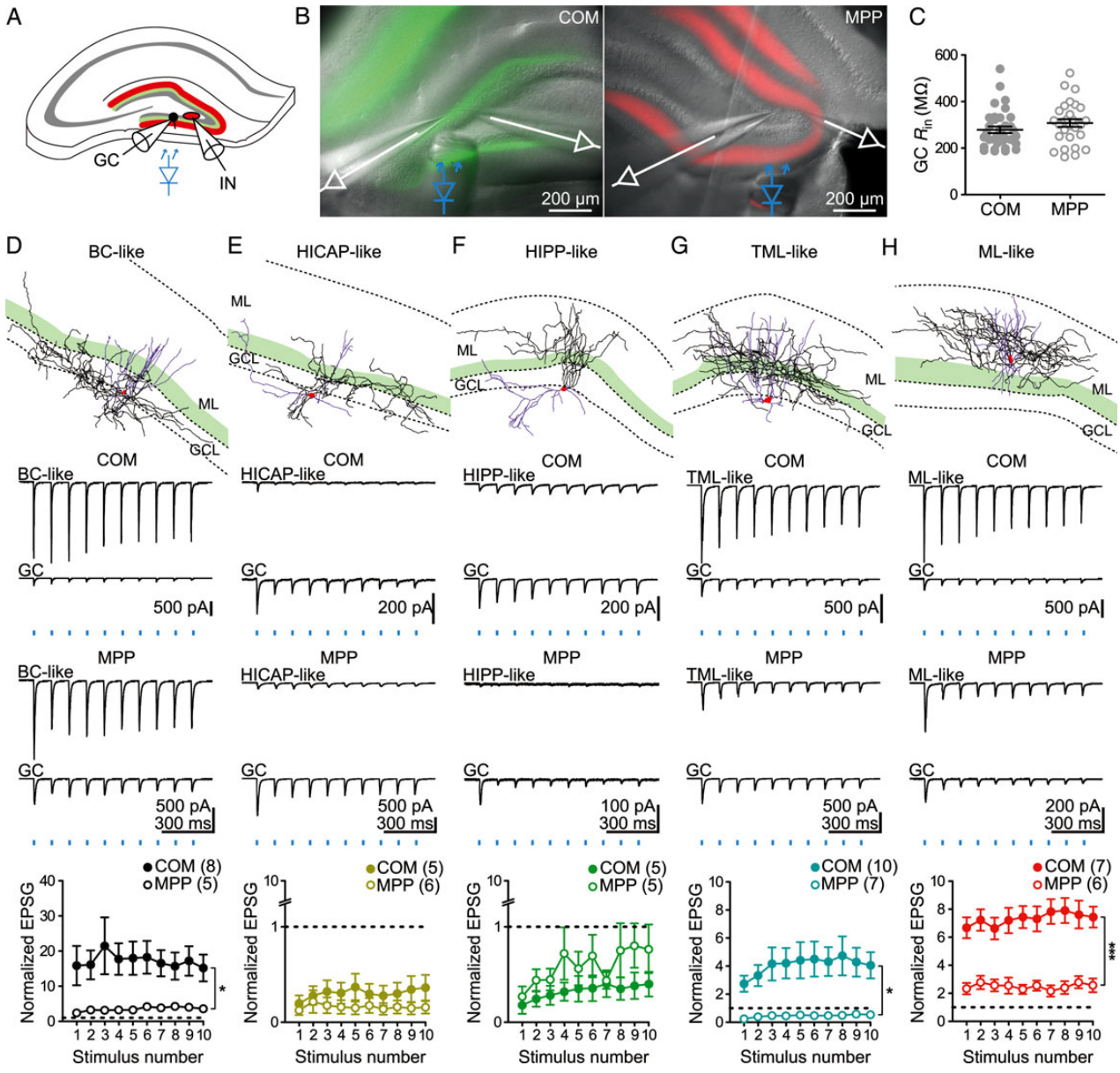

Figure 3. Target cell-specific synaptic efficacy at COM– and MPP–IN synapses. (*A*) Schematic diagram depicts the projections of COM (green) and MPP (red) and the area where dual whole-cell recordings were performed. (*B*) Dual whole-cell recordings of an IN and a GC during photostimulation of COM (green, left) or MPP (red, right) afferents in coronal hippocampal slices. (*C*) Scatter plot of R_{in} of all recorded GCs. (*D–H*) Comparison of light-evoked EPSCs between COM– and MPP–IN synapses. Top, exemplar reconstructions of recorded INs. Dendrites, soma, and axons are shown in magenta, red, and black, respectively. The IML (green zone) is outlined according to ChR2-eYFP expression of the same slice. Middle, averaged traces for each dual recording; 10 Hz photostimulation of either COM- (upper) or MPP- (lower) evoked EPSCs in an IN and a GC. EPSCs recorded in GCs are used to normalize the variability of ChR2 expression. Bottom, summary graphs show normalized EPSGs in each type of INs evoked by the COM and MPP. $^{*}P < 0.05$; $^{***}P < 0.001$. Numbers of cells are given in parentheses. Data are expressed as mean ± SEM.

BC-like cells were identified by their axonal arborizations being largely confined to the GCL (Fig. 3*D*, upper, 5/8 cells in the COM group and 3/5 cells in the MPP group were confirmed post hoc, based on morphology) and their characteristic fast-spiking pattern (8/8 cells in the COM group and 5/5 cells in the MPP group had a maximum firing rate of >80 Hz at 23 ± 2 °C). We found that both pathways evoked larger EPSCs in BC-like cells than in GCs during the 10-Hz photostimulation train. On average, the normalized EPSCs evoked by COM stimulation were greater than those by MPP stimulation (Fig. 3*D*, $n = 8$ in the COM group vs. $n = 5$ in the MPP group, $P = 0.029$, two-way repeated-measures ANOVA).

We next investigated the response properties of HICAP- and HIPP-like cells to COM and MPP stimulation, respectively. The axonal arborizations of HICAP-like cells were mainly confined to the IML (Fig. 3*E*, upper), whereas the arborizations of HIPP-like cells extended from the MML to the outer one-third of the ML (Fig. 3*F*, upper). Notably, both COM- and MPP-evoked EPSC amplitudes in HICAP- and HIPP-like cells were significantly smaller than in GCs during 10-Hz train photostimulation (Fig. 3*E*,*F*, middle). Unlike HICAP- and HIPP-like cells, TML-like cells, as reported previously [Soriano and Frotscher 1993; Mott et al. 1997; Hosp et al. 2014; termed atypical HIPP cells in Liu et al. (2014)], had their cell bodies located at the hilar–GCL border and

Table 2 Properties of EPSC in DG INs

Input	Synaptic delay[a] (ms)	20–80% Rise time[b] (ms)	Decay time constant[c] (ms)	Normalized conductance[d]
BC-like				
COM (8)	2.6 ± 0.1	0.4 ± 0.0	2.6 ± 0.3	14.8 ± 5.1
MPP (5)	4.3 ± 0.4	1.2 ± 0.2	5.5 ± 0.7	2.5 ± 0.6
HICAP-like				
COM (5)	2.9 ± 0.2	1.3 ± 0.3	6.7 ± 0.8	0.2 ± 0.1
MPP (6)	4.5 ± 1.1	1.8 ± 0.5	11.6 ± 0.8	0.1 ± 0.0
HIPP-like				
COM (5)	3.2 ± 0.2	1.0 ± 0.3	7.5 ± 1.6	0.2 ± 0.1
MPP (5)	5.2 ± 0.6	1.8 ± 0.3	8.9 ± 1.1	0.3 ± 0.1
TML-like				
COM (10)	2.9 ± 0.1	0.8 ± 0.1	6.9 ± 0.6	2.7 ± 0.6
MPP (7)	5.4 ± 1.3	1.8 ± 0.3	9.2 ± 1.8	0.3 ± 0.1
ML-like				
COM (7)	3.1 ± 0.2	0.8 ± 0.1	4.6 ± 0.4	6.6 ± 0.7
MPP (6)	4.1 ± 0.3	1.5 ± 0.1	6.6 ± 0.9	2.1 ± 0.4
GC				
COM (35)	3.1 ± 0.1	1.1 ± 0.1	5.7 ± 0.1	1.0 ± 0.0
MPP (29)	4.4 ± 0.2	2.1 ± 0.1	6.9 ± 0.2	1.0 ± 0.0

Note: Numbers of cells are given in parentheses.
[a]Synaptic delay was calculated as the time elapsed from the onset of photostimulation to the onset of first monosynaptic EPSC.
[b]20–80% rise time was measured from the first monosynaptic EPSC.
[c]Decay time constant was measured from the synaptic events that only contain monosynaptic EPSCs.
[d]First monosynaptic EPSG of the IN was normalized to that of the GC.

projected their axons throughout the entire ML (Fig. 3*G*, upper). Notably, TML-like cells responded differently to COM and MPP stimulation. TML-like cells received stronger input from the COM compared with GCs. However, the input strengths from the MPP to TML-like cells and to GCs were similar (Fig. 3*G*, middle and bottom). During 10-Hz repetitive stimulation, the normalized COM-evoked EPSGs were significantly greater than the normalized MPP-evoked EPSGs (Fig. 3*G*, middle, $n = 10$ in the COM group vs. $n = 7$ in the MPP group, $P = 0.0116$, two-way repeated-measures ANOVA). Finally, we identified a subpopulation of INs, hereafter called ML-like cells, which had their somatic location and axonal arborizations confined to the ML (Fig. 3*H*, upper). ML-like cells received a larger excitatory input from the COM compared with the MPP. The normalized EPSGs generated by the COM were always significantly larger than those generated by the MPP during 10-Hz train stimulation (Fig. 3*H*, $n = 7$ in the COM group vs. $n = 6$ in the MPP group, $P = 0.0003$, two-way repeated-measures ANOVA).

Taken together, COM- and MPP-mediated transmission onto INs is target cell-dependent. BC-, TML-, and ML-like cells received significantly stronger inputs from the COM relative to the MPP. In contrast, HICAP- and HIPP-like cells received relatively weak inputs from both afferents. Furthermore, target cell-specific facilitation and depression were observed in both COM and MPP pathways (see Supplementary Fig. 8). The heterogeneity of excitatory afferent inputs to INs suggests that the COM and MPP are likely to recruit different IN subpopulations.

TML- and ML-Like Cells Were Preferentially Recruited by the COM

Does the COM versus MPP recruit different IN subtypes? In addition to the heterogeneity of excitatory afferent inputs to INs, other properties such as membrane time constant (Buhl et al. 1996), input resistance (Khurana et al. 2011), EPSP kinetics (Maccaferri and Dingledine 2002), and the strength of inhibitory inputs (Banks et al. 2000) also affect EPSP-spike coupling. Here, we directly addressed spike transmission in 5 identified IN classes in the DG. Recordings were obtained in the cell-attached configuration to avoid interfering with the intracellular ionic composition. The spikes, detected as extracellular action currents, were recorded from the somata of dual-recorded INs and GCs (Fig. 4*A*,*B*). Following cell-attached recordings, we made biocytin-filled whole-cell recordings from the same cells and identified cell morphology post hoc. We first compared spike timings between GCs and INs in response to COM versus MPP photostimulation. In all sets of dual recordings, GCs exhibited a similar spike delay in response to COM versus MPP photostimulation (COM, 8.5 ± 0.9 ms, $n = 5$; Fig. 4*A* vs. MPP, 8.4 ± 0.7 ms, $n = 7$; Fig. 4*B*; $P = 0.7551$, Mann–Whitney rank-sum test). Relative to GC spike timing, BC-like cells generated spikes with a shorter delay (COM, 6.2 ± 0.5 ms, $n = 5$; Fig. 4*A* vs. MPP, 6.3 ± 0.6 ms, $n = 4$; Fig. 4*B*; $P = 1$, Mann–Whitney rank-sum test). In contrast, both HICAP- and HIPP-like cells showed a longer delay in response to either COM or MPP stimulation if they spiked (Fig. 4*A*,*B*). Notably, both TML- and ML-like cells showed differential responses to COM versus MPP stimulation. They exhibited a shorter spike delay in response to COM photostimulation (TML-like cell, 5.2 ± 0.5 ms, $n = 7$; Fig. 4*A*; ML-like cell, 4.6 ± 0.9 ms, $n = 4$; Fig. 4*A*) compared with that in response to MPP photostimulation (TML-like cell, 12.8 ± 1.4 ms, $n = 2$; Fig. 4*B*; ML-like cell, 9.7 ± 0.2 ms, $n = 3$; Fig. 4*B*).

We next compared the spike probabilities between GCs and INs by simultaneously dual recordings from a GC and an adjacent IN during 10-Hz train photostimulation. In all sets of dual recordings, the great majority (~71%) of GCs did not spike in response to 10-Hz train stimulation of either COM or MPP (Fig. 5*A*–*E*) and GCs that spiked exhibited a very low spike probability (ranging from 0 to 0.3). In contrast to GCs, BC-like cells (9 of 9 cells) displayed a high spike probability with a short latency in response to either COM or MPP stimulation (Fig. 5*A*). Unlike BC-like cells, HICAP- and HIPP-like cells generated significantly less spikes in response to either COM or MPP stimulation (Fig. 5*B*,*C*). TML- and ML-like cells showed

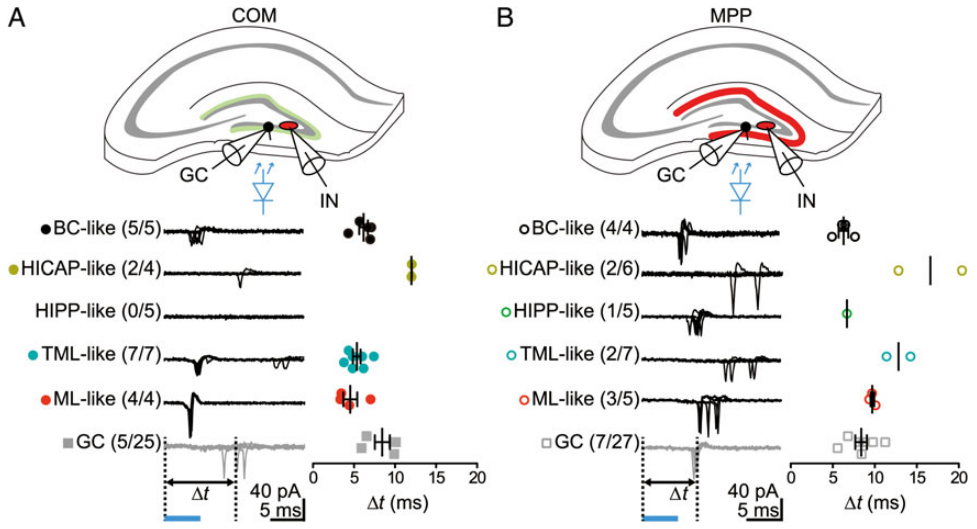

Figure 4. EPSP-spike coupling in INs and GCs. (*A*,*B*) Upper, schematic diagram showing photostimulation of either COM (*A*, green) or MPP (*B*, red) and recording configurations. Dual recordings were simultaneously made from INs and GCs. Lower, spike delay (Δt) in response to COM or MPP stimulation (blue bars). Left, example traces indicate extracellular action currents (6 superimposed sweeps) recorded from INs and GCs in the cell-attached, voltage-clamp mode. From top to bottom, traces from morphologically identified BC-, HICAP-, HIPP-, TML-, and ML-like cells and GCs. Right, averaged Δt for the COM (filled circles) and MPP (open circles). Numbers in parentheses represent recruited cell number/total recorded cell number.

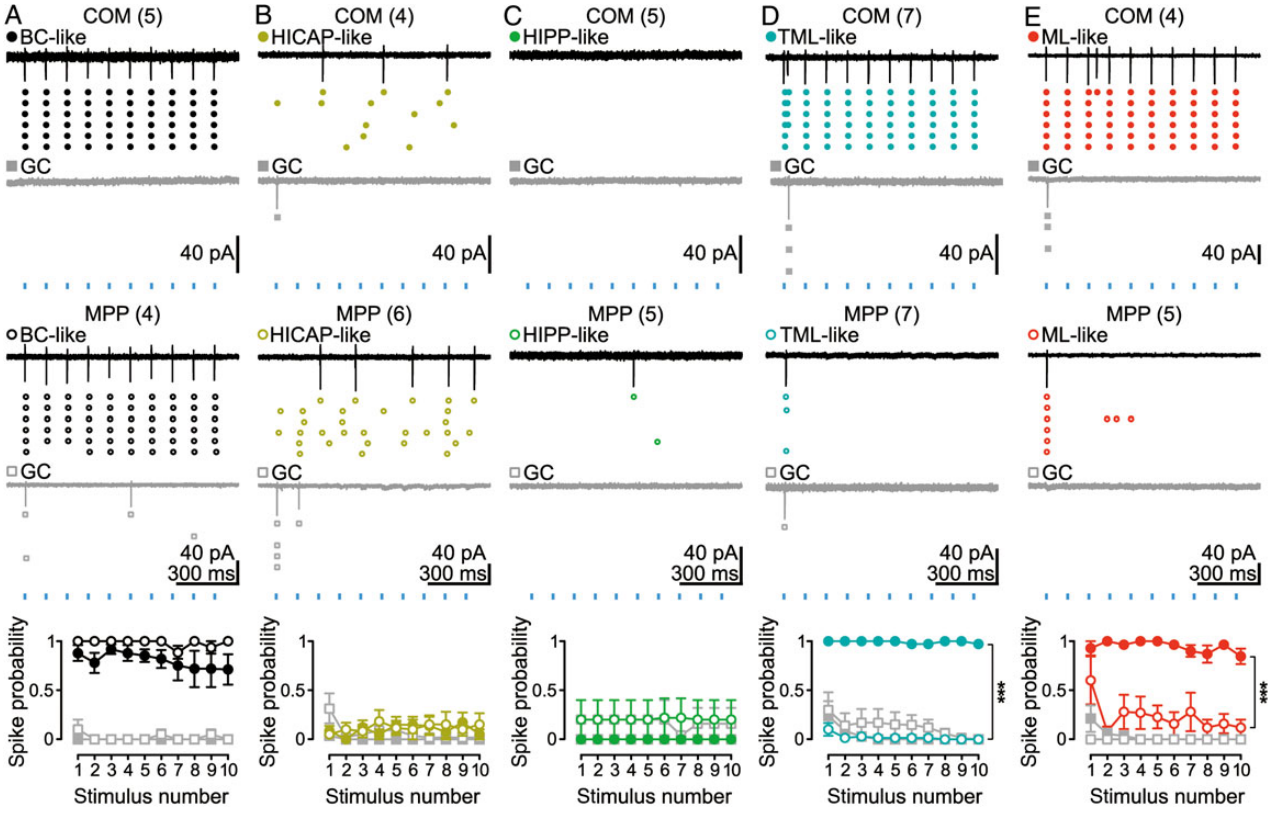

Figure 5. Differential recruitment of INs by the COM and MPP. (*A–E*) Spike probabilities of INs and GCs in response to 10 Hz photostimulation of COM or MPP. The light intensity that gave rise to saturated synaptic currents was applied here. Example traces indicate action currents recorded from INs and GCs. Spike raster plots below the traces show firing during 6 trials. Bottom, spike probabilities of INs and GCs. ***$P < 0.001$; numbers of cells are given in parentheses. Data are expressed as mean ± SEM.

strikingly different responses to COM versus MPP stimulation. Both TML- and ML-like cells reliably generated spikes with low failure rates in response to repeated COM stimulation (Fig. 5*D*,*E*). In contrast, both TML- and ML-like cells exhibited a low spike probability in response to MPP stimulation (Fig. 5*D*,*E*). Note that ML-like cells preferentially responded to the onset of train stimulation (Fig. 5*E*).

In summary, our data revealed input-specific recruitment of INs, which is a previously uncharacterized property of these cell types. Notably, the shorter spike delay of TML- and ML-like cells in response to COM stimulation (Fig. 4A) may account for the short EPSC–IPSC latency found at COM–GC synapses compared with MPP–GC synapses (Fig. 2*F*).

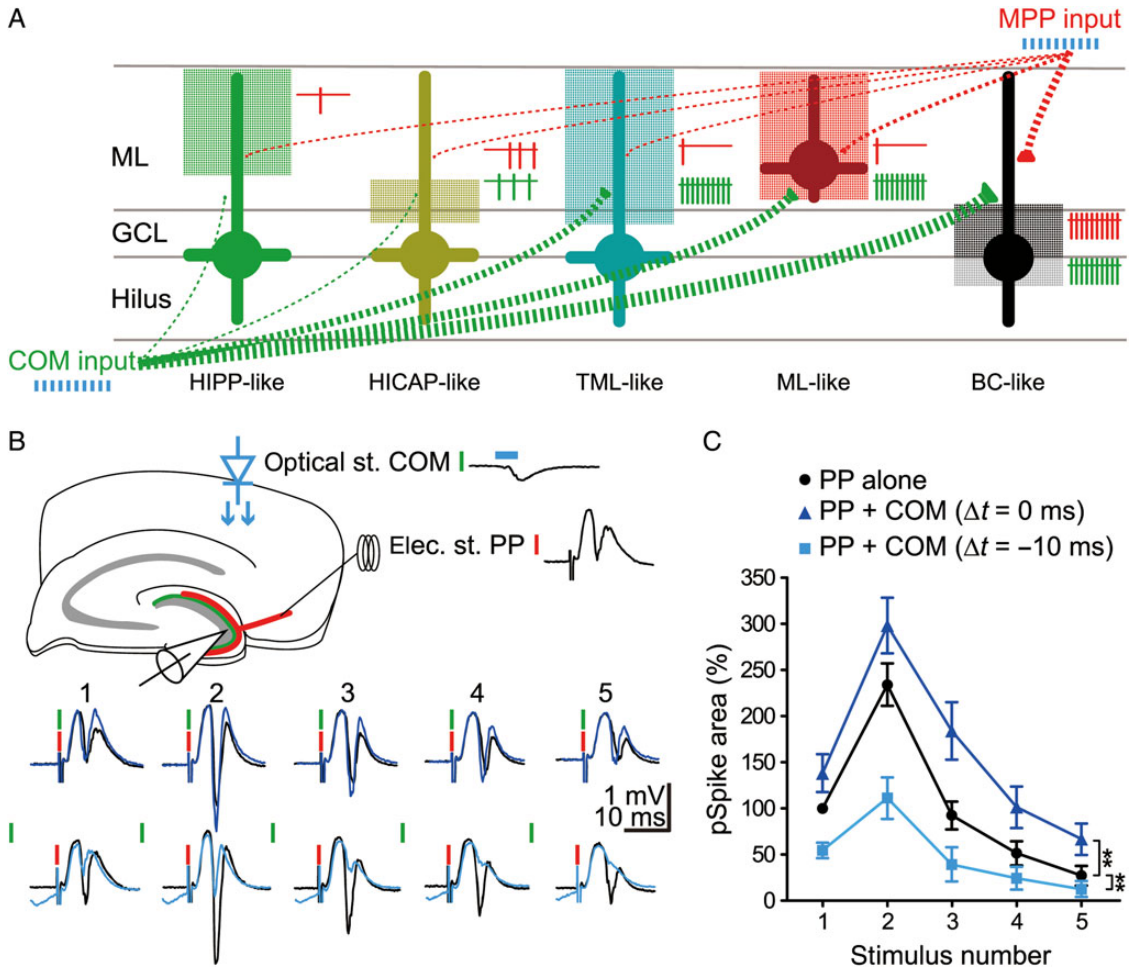

Figure 6. Summary of COM- and MPP-mediated neurotransmission, IN recruitment, and impact on GC activities. (*A*) Summary diagram of 5 distinct IN classes in the DG based on the morphological classification scheme. Filled circles mark the cell body location. The cell bodies give rise to thick lines indicating the dendritic trees. The hatched boxes are the domains where the axon of each IN primarily arborizes. Green and red dashed lines indicate the COM and MPP projections, respectively. Efficacy of COM- and MPP inputs to different INs types is represented by the dashed line thickness. Vertical ticks depict spikes in response to 10 Hz photostimulation (blue) of COM or MPP. (*B*) Top, schematic of experiment configuration: a field recording electrode was placed in the GCL to monitor pSpikes. A stimulation electrode was placed in the subiculum to activate the PP (red); the axonal fibers of COM (green) expressing ChR2 were stimulated with blue light. Each vertical bar represents a single-stimulating pulse. Bottom, pSpike responses to the PP and COM stimulation. Black traces, PP stimulation alone. Blue traces, simultaneous activation of PP and COM ($\Delta t = 0$ ms). Light blue traces, COM stimulation was delivered 10 ms before PP stimulation ($\Delta t = -10$ ms). (*C*) Summary of effect of COM activation on pSpike area, which reflects the number of GCs that spike synchronously to PP stimulation. The magnitude of pSpike area (normalized to the first pSpike area to PP alone) was plotted against the stimulation number. PP stimulation alone (PP alone) represents average from 10 recordings, and data points in the other 2 data sets represent average from 5 recordings. $^{**}P < 0.01$. Data are expressed as mean ± SEM.

Regulation of MPP Input Efficacy by COM Activation

As summarized in Figure 6A, TML-, ML-, and BC-like cells receive stronger excitatory input from the COM than the MPP. Furthermore, preferential recruitment of TML- and ML-like cells by the COM, but not by the MPP, likely contributes to the sustained high I/E ratios in GCs during 10-Hz train stimulation of COM (Fig. 2*I*). Finally, we determined the functional relevance of COM activation. We performed recordings of field potential in the GCL to monitor the population spike (pSpike) to PP stimulation, a primary excitatory input to the DG (Fig. 6*B*). The pSpike area is regarded as a measure of the number of GCs that spike synchronously to the input stimulus (Temprana et al. 2015). We tested the effect of COM activation at different timing relative to the cortical input on the GC pSpikes at higher temperature. At 34 °C, bursts of 5 electrical shocks at 10 Hz applied to the PP alone elicited pSpikes recorded in the GCL (Fig. 6*B*, black). Notably, concurrent activation of COM by photostimulation increased the pSpike areas (Fig. 6*B*, blue and *C*). In contrast, pSpike areas to PP activation were greatly decreased when the COM was activated 10 ms before the PP (Fig. 6*B*, light blue and *C*). Thus, activation of COM at behaviorally relevant frequency can gate cortical information flow, depending on the temporal relationship between the COM and the MPP (Fig. 6*C*).

Discussion

The hilar COM is known to exert a suppressive effect on GC discharge via the activation of local INs in the DG (Buzsáki and Czéh 1981; Buzsáki and Eidelberg 1981; Bilkey and Goddard 1987). To date, the cellular targets of the hilar COM remain mostly unknown. Our study directly addressed this long-lasting question in hippocampal physiology. Using cell type-specific optogenetic tools, we found that COM activation caused substantially greater inhibition in GCs, through preferential recruitment of TML- and ML-like cells compared with MPP activation.

The DG integrates information from multiple brain regions, including the entorhinal cortex via the PP, the contralateral hilus via the commissural fibers, the medial septum via the septohippocampal pathway (Bilkey and Goddard 1987), and the SuM via the SuM–hippocampal pathway (Soussi et al. 2010). Relative to input afferents from the entorhinal cortex, investigations of synaptic transmission of hilar MCs and SuM neurons onto GCs are notably scarce. To some extent, the relative neglect of these 2 inputs is explained by the great overlap of their axonal fibers in the IML (Boulland et al. 2009; Soussi et al. 2010; Kohara et al. 2014). It is, therefore, impossible to selectively activate only one of them using conventional electrical stimulation. With selective ChR2 expression in the COM, we were able to stimulate the axonal fibers expressing light-activated channel, ChR2 and dissect its circuit function. However, a potential complication associated with the use of AAV-ChR2 is the artificial synaptic depression reported in some cases (Zhang and Oertner 2007; Cruikshank et al. 2010; Jackman et al. 2014). With our experimental condition, this possibility is minimal and if any, it does not alter the main conclusion. First, we found that synaptic transmission evoked by electrical stimulation at the CA3–CA1 synapse, a well-characterized synapse, exhibits similar dynamics as that evoked by optical stimulation (see Supplementary Fig. 9). These findings are contrary to a recent report by Jackman et al. (2014). Second, fiber volley recordings from the IML showed that 10 Hz photostimulation evokes relatively reliable presynaptic axonal firing with only a transient depression in the initial responses (see Supplementary Fig. 10). Third, the light-evoked, normalized EPSGs (~2-fold) obtained at MPP–ML-like cell synapses (Fig. 3*H*) in this study are similar to those measured at PP–molecular layer PP-associated cell (MOPP) synapses evoked by electrical stimulation (Li et al. 2013). Finally, if any artificial synaptic depression at COM–IN synapses should be taken into account, our results would rather support the conclusion that the COM, compared with the MPP, can more reliably activate TML- and ML-like cells.

Consistent with previous studies using electrical stimulation (Ewell and Jones 2010; Dieni et al. 2013), photostimulation of MPP at 10 Hz caused rapid reduction in IPSGs, resulting in decreases in I/E ratios. Recruitment of specific IN subpopulations by the MPP likely accounts for this depression. As illustrated in Figure 5, photostimulation of MPP reliably recruited BC-like cells, whereas ML-like cells were transiently activated during the onset of 10-Hz train stimulation. Therefore, the initial MPP-driven inhibition onto GCs arises from both IN subpopulations, but the sustained inhibition is solely contributed by BC-like cells. Previous studies (Kraushaar and Jonas 2000; Liu et al. 2014) have shown that the dynamics of BC–GC synapses exhibit frequency-dependent depression. Therefore, those findings explain the rapid reduction in I/E ratios observed in the present study since BCs are the main contributor to MPP-driven inhibition to GCs under our stimulation paradigm. Contrary to MPP activation, COM stimulation exhibits greater inhibition in GCs, resulting in marked increases in I/E ratios. Notably, COM activation not only recruits BC-like cells, but also reliably recruits TML- and ML-like cells throughout the entire 10-Hz train stimulation. Consistent with the sustained high I/E ratios during spike train, TML-like cell to GC cell synapses exhibited less or no depression at 10 Hz (see Supplementary Fig. 11). Thus, the activation of TML- and ML-like cells during repetitive input activity likely accounts for increasing I/E ratios in COM-driven inhibition.

It is important to note that not all BC-like cells in this study were identified on the basis of their morphological features. Five of 13 cells were identified as BC-like cells by the characteristic fast-spiking patterns because of incomplete recovery of axonal arborization. Therefore, axo-axonic cells (AACs), which also display high-frequency action potential firing, are likely included in the present study (Weng et al. 2010; Liu et al. 2014). Among all morphological identified fast-spiking INs, we found an AAC-like cell (1/13 cells; see Supplementary Fig. 12), which displayed the vertical rows of several boutons called "cartridges" along the putative axon initial segment of GCs (see Supplementary Fig. 12*B*). Likewise, ML-like cells defined here may include MOPP cells and neurogliaform cells. Both of them are shown to form functional synapses with GCs and contribute to feedforward inhibition onto GCs (Armstrong et al. 2011; Li et al. 2013). However, we only identified a single putative neurogliaform cell (1/14 cells), which showed typical axon projections across the fissure into the CA1 region (Armstrong et al. 2011) and was not included in this study. Finally, all INs with their axon projection to the outer ML (OML) in this study were classified as HIPP-like cells. Although original description of HIPP cells found the dendrites restricted in the hilus (Han et al. 1993), our recent study (Liu et al. 2014) showed that a large proportion of HIPP-like cells, which project their axons to the OML, have the dendritic arbor in the ML [also see Hosp et al. (2014)]. In keeping with this notion, we observed that all HIPP-like cells (10 cells) in this study display their dendrites outside the hilus.

Our results show that various IN types (except BC-like cells) are differentially activated by different afferent pathways, suggesting that different IN types selectively mediate segregation of information flow. It seems that reliable recruitment of BC-like cells by both COM and MPP is ascribed to the strong excitatory drive, which overcomes the poor synaptic integration properties (Hu et al. 2014). It is worth noting that HIPP- and HICAP-like cells exert highly dynamic inhibition onto dendritic parts of GCs (Liu et al. 2014). They generate weak inhibition onto GCs when they fire sparsely. However, they generate powerful and reliable inhibitory output when they are switched from the single to the burst spiking mode (Liu et al. 2014). This gives rise to an interesting question: How are HIPP- and HICAP-like cells activated in the context of extrinsic afferent systems? To answer this question, systematic investigations of other subcortical afferents to these INs are indispensable. These systems mainly include afferents originating from the medial septum/diagonal band of Broca GABAergic and cholinergic neurons, neurochemically distinct types of neurons located in the SuM area, serotonergic fibers from the median raphe, noradrenergic afferents from the pontine nucleus and locus coeruleus, dopamine axons originating in the ventral tegmental area, and the commissural projection system (Leranth and Hajszan 2007). Overall, extrahippocampal and intrahippocampal excitatory input-specific recruitment of certain IN subpopulations may underscore a "division of labor" in cortical circuits, where distinct computational functions are implemented by various types of local inhibitory INs.

It is also important to point out that some limitations exist in the present study for the understanding of COM-mediated neurotransmission. First, selective COM targeting depends on the efficacy of the *Grik4-cre* mouse line and Cre-dependent expression of AAV-ChR2. Interestingly, a previous study reports that calretinin-negative MCs in the dorsal DG are preferentially manipulated by this method, whereas the ventral calretinin-positive MCs are less affected (Nakazawa et al. 2002). It is also noted that MCs not only exhibit the difference in calretinin immunoreactivity along the dorsoventral axis, but also vary in complexity of thorny excrescences, synaptic responses, and their intrinsic properties (Blasco-Ibáñez and Freund 1997; Fujise et al. 1998; Jinno et al. 2003). These observations suggest that different MC subpopulations along the axis might play various physiological roles. To further

elaborate the functional characteristics of the COM, targeting MCs using different Cre lines, for example, the MC/CA3-cre #4688 line (Jinde et al. 2012), may be helpful in further specifying the function of COM-mediated transmission. Second, most of our study focused on COM-mediated transmission to the contralateral dorsal DG, although we noted that the COM projects along the entire longitudinal axis of the contralateral DG. Whether the synaptic transmission of COM–ventral DG and COM–dorsal DG differs functionally remains an interesting question. Moreover, the functions of the hippocampus are not equal along the hippocampal longitudinal axis (Strange et al. 2014). For example, there is a gradual enlargement of place-field scale along the dorsoventral axis (Kjelstrup et al. 2008). Therefore, the role of the COM in coordinating different functional modalities in different hippocampal transverse units demands extensive investigations.

Despite the above-mentioned limitations, our study provides evidence about the source of COM-mediated inhibitory control over GCs and supports the in vivo observation that GCs exhibit hyperexcitability in response to PP stimulation after MCs were ablated extensively throughout the entire longitudinal axis (Jinde et al. 2012). Some functional correlations were associated with hyperexcitable GCs, including increased theta power of DG local field potentials, elevated anxiety, and impaired contextual discrimination (Jinde et al. 2012). Further experiments using temporally precise tools to excite or silence the COM in vivo during behavioral tasks are required.

Supplementary Material

Supplementary material can be found at: http://www.cercor.oxfordjournals.org/.

Funding

This work was supported by grants from the Ministry of Education, Aim for the Top University Plan, National Health Research Institutes (NHRI-EX104-10105NI), and the Taiwan Ministry of Science and Technology (MOST 102-2321-B-010-019; 103-2321-B-010-010; and 100-2320-B-010-014-MY3).

Notes

We thank M.M. Poo for critically reading the manuscript, Y.C. Liu and Y.C. Lin for commenting on an earlier version of this manuscript, and members of the Lien laboratory for discussions on the data. *Conflict of Interest*: None declared.

References

Alme CB, Buzzetti RA, Marrone DF, Leutgeb JK, Chawla MK, Schaner MJ, Bohanick JD, Khoboko T, Leutgeb S, Moser EI, et al. 2010. Hippocampal granule cells opt for early retirement. Hippocampus. 20:1109–1123.

Amaral DG, Scharfman HE, Lavenex P. 2007. The dentate gyrus: fundamental neuroanatomical organization (dentate gyrus for dummies). Prog Brain Res. 163:3–22.

Armstrong C, Szabadics J, Tamás G, Soltesz I. 2011. Neurogliaform cells in the molecular layer of the dentate gyrus as feed-forward γ-aminobutyric acidergic modulators of entorhinal-hippocampal interplay. J Comp Neurol. 519:1476–1491.

Banks MI, White JA, Pearce RA. 2000. Interactions between distinct $GABA_A$ circuits in hippocampus. Neuron. 25:449–457.

Bartos M, Alle H, Vida I. 2011. Role of microcircuit structure and input integration in hippocampal interneuron recruitment and plasticity. Neuropharmacology. 60:730–739.

Behr J, Lyson KJ, Mody I. 1998. Enhanced propagation of epileptiform activity through the kindled dentate gyrus. J Neurophysiol. 79:1726–1732.

Bilkey DK, Goddard GV. 1987. Septohippocampal and commissural pathways antagonistically control inhibitory interneurons in the dentate gyrus. Brain Res. 405:320–325.

Blasco-Ibáñez JM, Freund TF. 1997. Distribution, ultrastructure, and connectivity of calretinin-immunoreactive mossy cells of the mouse dentate gyrus. Hippocampus. 7:307–320.

Boulland JL, Jenstad M, Boekel AJ, Wouterlood FG, Edwards RH, Storm-Mathisen J, Chaudhry FA. 2009. Vesicular glutamate and GABA transporters sort to distinct sets of vesicles in a population of presynaptic terminals. Cereb Cortex. 19:241–248.

Buckmaster PS, Wenzel HJ, Kunkel DD, Schwartzkroin PA. 1996. Axon arbors and synaptic connections of hippocampal mossy cells in the rat *in vivo*. J Comp Neurol. 366:271–292.

Buhl EH, Szilágyi T, Halasy K, Somogyi P. 1996. Physiological properties of anatomically identified basket and bistratified cells in the CA1 area of the rat hippocampus *in vitro*. Hippocampus. 6:294–305.

Buzsáki G, Czéh G. 1981. Commissural and perforant path interactions in the rat hippocampus. Field potentials and unitary activity. Exp Brain Res. 43:429–438.

Buzsáki G, Eidelberg E. 1981. Commissural projection to the dentate gyrus of the rat: evidence for feed-forward inhibition. Brain Res. 230:346–350.

Chancey JH, Poulsen DJ, Wadiche JI, Overstreet-Wadiche L. 2014. Hilar mossy cells provide the first glutamatergic synapses to adult-born dentate granule cells. J Neurosci. 34:2349–2354.

Chiang PH, Wu PY, Kuo TW, Liu YC, Chan CF, Chien TC, Cheng JK, Huang YY, Chiu CD, Lien CC. 2012. GABA is depolarizing in hippocampal dentate granule cells of the adolescent and adult rats. J Neurosci. 32:62–67.

Coulter DA, Carlson GC. 2007. Functional regulation of the dentate gyrus by GABA-mediated inhibition. Prog Brain Res. 163:235–243.

Cruikshank SJ, Urabe H, Nurmikko AV, Connors BW. 2010. Pathway-specific feedforward circuits between thalamus and neocortex revealed by selective optical stimulation of axons. Neuron. 65:230–245.

Dieni CV, Nietz AK, Panichi R, Wadiche JI, Overstreet-Wadiche L. 2013. Distinct determinants of sparse activation during granule cell maturation. J Neurosci. 33:19131–19142.

Ewell LA, Jones MV. 2010. Frequency-tuned distribution of inhibition in the dentate gyrus. J Neurosci. 30:12597–12607.

Freund TF, Buzsáki G. 1996. Interneurons of the hippocampus. Hippocampus. 6:347–470.

Fujise N, Liu Y, Hori N, Kosaka T. 1998. Distribution of calretinin immunoreactivity in the mouse dentate gyrus: II. Mossy cells, with special reference to their dorsoventral difference in calretinin immunoreactivity. Neuroscience. 82:181–200.

Han ZS, Buhl EH, Lörinczi Z, Somogyi P. 1993. A high degree of spatial selectivity in the axonal and dendritic domains of physiologically identified local-circuit neurons in the dentate gyrus of the rat hippocampus. Eur J Neurosci. 5:395–410.

Hosp JA, Strüber M, Yanagawa Y, Obata K, Vida I, Jonas P, Bartos M. 2014. Morpho-physiological criteria divide dentate gyrus interneurons into classes. Hippocampus. 24:189–203.

Hu H, Gan J, Jonas P. 2014. Interneurons. Fast-spiking, parvalbumin$^+$ GABAergic interneurons: from cellular design to microcircuit function. Science. 345:1255–1263.

Jackman SL, Beneduce BM, Drew IR, Regehr WG. 2014. Achieving high-frequency optical control of synaptic transmission. J Neurosci. 34:7704–7714.

Jinde S, Zsiros V, Jiang Z, Nakao K, Pickel J, Kohno K, Belforte JE, Nakazawa K. 2012. Hilar mossy cell degeneration causes transient dentate granule cell hyperexcitability and impaired pattern separation. Neuron. 76:1189–1200.

Jinno S, Ishizuka S, Kosaka T. 2003. Ionic currents underlying rhythmic bursting of ventral mossy cells in the developing mouse dentate gyrus. Eur J Neurosci. 17:1338–1354.

Khurana S, Remme MW, Rinzel J, Golding NL. 2011. Dynamic interaction of Ih and IK-LVA during trains of synaptic potentials in principal neurons of the medial superior olive. J Neurosci. 31:8936–8947.

Kjelstrup KB, Solstad T, Brun VH, Hafting T, Leutgeb S, Witter MP, Moser EI, Moser MB. 2008. Finite scale of spatial representation in the hippocampus. Science. 321:140–143.

Kohara K, Pignatelli M, Rivest AJ, Jung HY, Kitamura T, Suh J, Frank D, Kajikawa K, Mise N, Obata Y, et al. 2014. Cell type-specific genetic and optogenetic tools reveal hippocampal CA2 circuits. Nat Neurosci. 17:269–279.

Kraushaar U, Jonas P. 2000. Efficacy and stability of quantal GABA release at a hippocampal interneuron-principal neuron synapse. J Neurosci. 20:5594–5607.

Krueppel R, Remy S, Beck H. 2011. Dendritic integration in hippocampal dentate granule cells. Neuron. 71:512–528.

Lee S, Kruglikov I, Huang ZJ, Fishell G, Rudy B. 2013. A disinhibitory circuit mediates motor integration in the somatosensory cortex. Nat Neurosci. 16:1662–1670.

Leranth C, Hajszan T. 2007. Extrinsic afferent systems to the dentate gyrus. Prog Brain Res. 163:63–84.

Leutgeb JK, Leutgeb S, Moser MB, Moser EI. 2007. Pattern separation in the dentate gyrus and CA3 of the hippocampus. Science. 315:961–966.

Li Y, Stam FJ, Aimone JB, Goulding M, Callaway EM, Gage FH. 2013. Molecular layer perforant path-associated cells contribute to feed-forward inhibition in the adult dentate gyrus. Proc Natl Acad Sci USA. 110:9106–9111.

Liu YC, Cheng JK, Lien CC. 2014. Rapid dynamic changes of dendritic inhibition in the dentate gyrus by presynaptic activity patterns. J Neurosci. 34:1344–1357.

Maccaferri G, Dingledine R. 2002. Control of feedforward dendritic inhibition by NMDA receptor-dependent spike timing in hippocampal interneurons. J Neurosci. 22:5462–5472.

Mott DD, Turner DA, Okazaki MM, Lewis DV. 1997. Interneurons of the dentate-hilus border of the rat dentate gyrus: morphological and electrophysiological heterogeneity. J Neurosci. 17:3990–4005.

Nakazawa K, Quirk MC, Chitwood RA, Watanabe M, Yeckel MF, Sun LD, Kato A, Carr CA, Johnston D, Wilson MA, et al. 2002. Requirement for hippocampal CA3 NMDA receptors in associative memory recall. Science. 297:211–218.

Pernía-Andrade AJ, Jonas P. 2014. Theta-gamma-modulated synaptic currents in hippocampal granule cells in vivo define a mechanism for network oscillations. Neuron. 81:140–152.

Scharfman HE, Myers CE. 2013. Hilar mossy cells of the dentate gyrus: a historical perspective. Front Neural Circuits. 6:106.

Schmidt-Hieber C, Jonas P, Bischofberger J. 2004. Enhanced synaptic plasticity in newly generated granule cells of the adult hippocampus. Nature. 429:184–187.

Schmidt-Hieber C, Jonas P, Bischofberger J. 2007. Subthreshold dendritic signal processing and coincidence detection in dentate gyrus granule cells. J Neurosci. 27:8430–8441.

Soriano E, Frotscher M. 1993. GABAergic innervation of the rat fascia dentata: a novel type of interneuron in the granule cell layer with extensive axonal arborization in the molecular layer. J Comp Neurol. 334:385–396.

Soriano E, Frotscher M. 1994. Mossy cells of the rat fascia dentata are glutamate-immunoreactive. Hippocampus. 4:65–69.

Soussi R, Zhang N, Tahtakran S, Houser CR, Esclapez M. 2010. Heterogeneity of the supramammillary-hippocampal pathways: evidence for a unique GABAergic neurotransmitter phenotype and regional differences. Eur J Neurosci. 32:771–785.

Strange BA, Witter MP, Lein ES, Moser EI. 2014. Functional organization of the hippocampal longitudinal axis. Nat Rev Neurosci. 15:655–669.

Temprana SG, Mongiat LA, Yang SM, Trinchero MF, Alvarez DD, Kropff E, Giacomini D, Beltramone N, Lanuza GM, Schinder AF. 2015. Delayed coupling to feedback inhibition during a critical period for the integration of adult-born granule cells. Neuron. 85:116–130.

Treves A, Tashiro A, Witter MP, Moser EI. 2008. What is the mammalian dentate gyrus good for? Neuroscience. 154:1155–1172.

Vivar C, Potter MC, Choi J, Lee JY, Stringer TP, Callaway EM, Gage FH, Suh H, van Praag H. 2012. Monosynaptic inputs to new neurons in the dentate gyrus. Nat Commun. 3:1107.

Weng JY, Lin YC, Lien CC. 2010. Cell type-specific expression of acid-sensing ion channels in hippocampal interneurons. J Neurosci. 30:6548–6558.

West JR, Nornes HO, Barnes CL, Bronfenbrenner M. 1979. The cells of origin of the commissural afferents to the area dentata in the mouse. Brain Res. 160:203–215.

Yizhar O, Fenno LE, Davidson TJ, Mogri M, Deisseroth K. 2011. Optogenetics in neural systems. Neuron. 71:9–34.

Zhang YP, Oertner TG. 2007. Optical induction of synaptic plasticity using a light-sensitive channel. Nat Methods. 4:139–141.